

# An atomic-scale view of single-site Pt catalysis for low-temperature CO oxidation

Andrew J. Therrien<sup>1</sup>, Alyssa J. R. Hensley<sup>®</sup><sup>2</sup>, Matthew D. Marcinkowski<sup>1</sup>, Renqin Zhang<sup>®</sup><sup>2</sup>, Felicia R. Lucci<sup>1</sup>, Benjamin Coughlin<sup>1</sup>, Alex C. Schilling<sup>1</sup>, Jean-Sabin McEwen<sup>®</sup><sup>2,3,4,5\*</sup> and E. Charles H. Sykes<sup>®</sup><sup>1\*</sup>

Single-atom catalysts have attracted great attention in recent years due to their high efficiencies and cost savings. However, there is debate concerning the nature of the active site, interaction with the support, and mechanism by which single-atom catalysts operate. Here, using a combined surface science and theory approach, we designed a model system in which we unambiguously show that individual Pt atoms on a well-defined Cu<sub>2</sub>O film are able to perform CO oxidation at low temperatures. Isotopic labelling studies reveal that oxygen is supplied by the support. Density functional theory rationalizes the reaction mechanism and confirms X-ray photoelectron spectroscopy measurements of the neutral charge state of Pt. Scanning tunnelling microscopy enables visualization of the active site as the reaction progresses, and infrared measurements of the CO stretch frequency are consistent with atomically dispersed Pt atoms. These results serve as a benchmark for characterizing, understanding and designing other single-atom catalysts.

upported single atoms are a new class of catalyst in which precious metals can be used at the ultimate efficiency limit. Singleatom catalysis begins to merge the fields of homogeneous and heterogeneous catalysis, maintaining the tunability of homogeneous catalysts and the ease of product separation and robustness of heterogeneous catalysts<sup>1-3</sup>. However, despite many recent studies of single-atom heterogeneous catalysts, there has been considerable debate regarding the catalytic capabilities of supported single atoms. While some studies show supported single atoms as active catalytic centres<sup>3-8</sup>, others claim nanoparticles to be the active species in similar systems<sup>9-11</sup>. There is also a lack of evidence that carefully engineered single atoms remain dispersed under reaction conditions. Thus, the question arises: 'Are supported single atoms reactive?' Furthermore, if single atoms are active, questions remain about their stability, how they bind to the support, and their charge state. Due to the inherent complexity of heterogeneous catalysts, it is difficult to fully characterize the structure and environment surrounding single atoms in a supported catalyst, which are critical for accurate modelling, understanding, and the design of new singleatom catalysts. For this reason, model studies of supported single atoms are required to investigate the atomic-scale geometric and electronic properties that define their catalytic behaviour. This realization has motivated surface science studies featuring scanning tunnelling microscopy (STM) and other techniques to examine the structure and stability of supported single atoms<sup>12,13</sup>, their charge state<sup>14-17</sup>, and the adsorption of probe molecules such as CO<sup>18-21</sup>. While the catalytic activity of small clusters has been visualized by STM<sup>22,23</sup>, a full-picture of adsorption and reaction at supported single atoms is currently lacking.

In this work, a detailed description of the geometric structure, electronic structure, and reaction mechanism at single Pt atoms is presented through a combination of surface science, microscopy and theory. The reaction of interest is low-temperature CO oxidation, which is central to the previously mentioned debates<sup>1-11</sup>. The reaction

is performed with single Pt atoms supported on the '29' copper oxide surface, which is a  $\text{Cu}_2\text{O}(111)$ -like single-layer film grown on Cu(111) that has been previously modelled and described<sup>24,25</sup>.

### Results

Characterization of Pt atom dispersion on copper oxide film. When small amounts of Pt are added to the '29' oxide surface, they remain atomically dispersed, as found by CO reflection absorption infrared spectroscopy (RAIRS) and high-resolution STM (Fig. 1). The RAIRS data in Fig. 1a show CO stretching bands for various Pt coverages at 265 K. At this temperature, CO has completely desorbed from the oxide support and all the signal is due to CO on Pt sites<sup>25</sup>. Starting at the high Pt coverage of 40% of a monolayer, the spectrum is indicative of Pt nanoparticle growth, closely resembling highly stepped extended Pt surfaces with a broad 2,065 cm<sup>-1</sup> CO stretch band<sup>9,26-28</sup>. For samples made with the Pt coverage decreased to 10% of a monolayer, the peak shifts to lower wavenumbers due to decreasing dipole-dipole coupling between CO molecules<sup>26</sup> and heterogeneity in the binding sites for CO on Pt nanoparticles<sup>29</sup>, which is a trend that has previously been modelled by density functional theory (DFT)<sup>28</sup>. At a Pt coverage of 6% of a monolayer, the peak due to CO on Pt particles continues to shift; however, a shoulder at 2,028 cm<sup>-1</sup> can be seen, which is highlighted by the dotted red line. As the Pt coverage is decreased to 4% of a monolayer, it is clear that there are two peaks: one at 2,045 cm<sup>-1</sup> for Pt particles and one at 2,028 cm<sup>-1</sup> for single Pt atoms. At a Pt coverage of 2% of a monolayer, the only peak present is at 2,028 cm<sup>-1</sup>. The peak has a narrow full width at half maximum of 10 cm<sup>-1</sup>, indicating exclusive formation of Pt single atoms at uniform surface sites<sup>30</sup>, as confirmed by STM in Fig. 1b. Likewise, at a Pt coverage of 1% of a monolayer, only a single peak at 2,028 cm<sup>-1</sup> is seen. Another strong indication that Pt is atomically dispersed at a Pt coverage of 2% of a monolayer and below is the fixed CO stretch frequency with respect to Pt coverage when the Pt sites are saturated by CO. This lack of lateral

<sup>1</sup>Department of Chemistry, Tufts University, Medford, MA, USA. <sup>2</sup>The Gene and Linda Voiland School of Chemical Engineering and Bioengineering, Washington State University, Pullman, WA, USA. <sup>3</sup>Department of Physics and Astronomy, Washington State University, Pullman, WA, USA. <sup>4</sup>Department of Chemistry, Washington State University, Pullman, WA, USA. <sup>5</sup>Institute for Integrated Catalysis, Pacific Northwest National Laboratory, Richland, WA, USA. \*e-mail: js.mcewen@wsu.edu; charles.sykes@tufts.edu

ARTICLES NATURE CATALYSIS

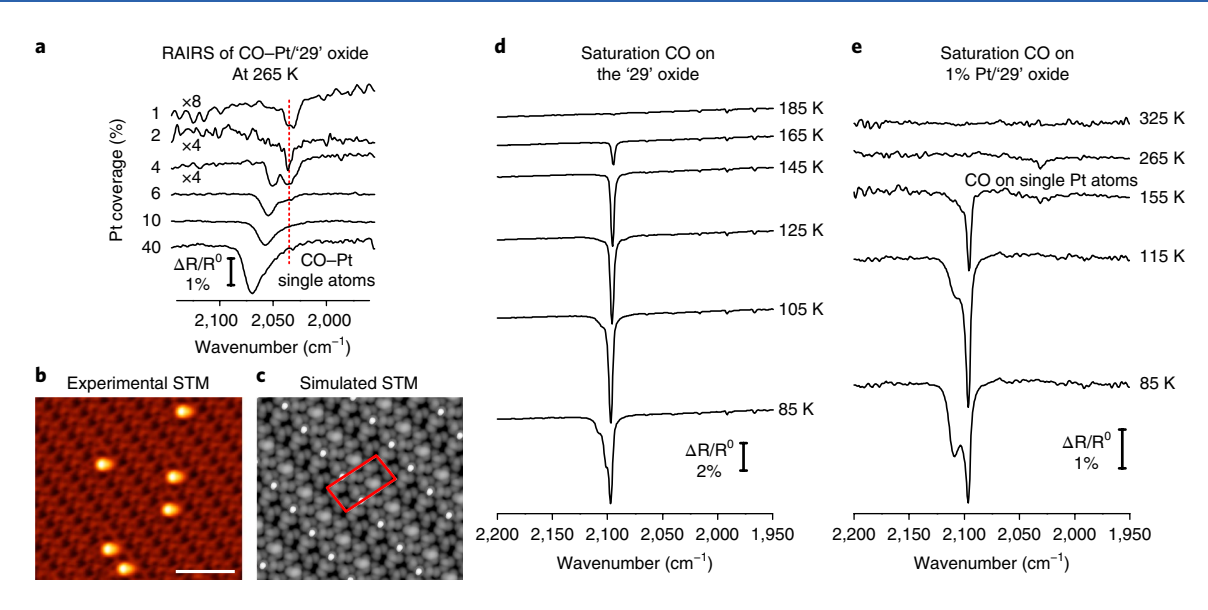


**Fig. 1 | Characterization of CO stretch frequencies at Pt single atoms and nanoparticles. a**, RAIRS data of the CO stretch at various Pt coverages at 265 K, where R is reflectance. **b**, High-resolution STM of a 0.5% of a monolayer Pt coverage on the '29' copper oxide after adding CO and annealing to 250 K. Scale bar: 5 nm. **c**, Simulated STM image at -0.5 V of the DFT model with a CO-Pt complex in each unit cell (red border). **d,e**, RAIRS data from an initial CO saturation coverage annealed to various temperatures on the '29' oxide, (**d**) and with a 1% Pt monolayer coverage on the '29' oxide (**e**).

CO-CO interactions is due to the high dispersion of the single Pt atoms and is in contrast with the shifts observed in the CO stretch on Pt particles. These findings are in line with CO stretching frequencies reported on small Pt clusters and single atoms and serve as benchmarks to deconvolute the infrared data for complex multicomponent heterogeneous catalysts<sup>2,9,31</sup>. Furthermore, the existence of only one RAIRS band indicates that there is one CO per Pt atom, as dicarbonyl species exhibit two bands. DFT calculations confirm that a dicarbonyl species is unlikely to be present (Supplementary Fig. 1)30,32. As shown in Fig. 1b, STM imaging verifies the assignment of highly dispersed Pt atoms bound to a single CO, as the CO-Pt features appear symmetrical and atomically sized, which is not expected of dicarbonyl species 19-21,33. This assignment is further verified by the match with the DFT simulated STM image in appearance and location of the CO-Pt units on the '29' oxide<sup>24,25</sup>, which is shown in Fig. 1c.

To investigate the change in CO stretch frequencies with CO coverage, RAIRS data were collected at several surface temperatures. As shown in Fig. 1d, a bare '29' oxide surface was saturated with CO at 85 K, resulting in CO stretching bands around 2,100 cm<sup>-1</sup>. The peaks are in good agreement with CO bound to bulk Cu<sub>2</sub>O(111) and similar Cu<sub>2</sub>O/Cu(111) surfaces<sup>34–36</sup>. As the surface is heated, CO desorbs from different sites, leaving behind a final peak at 2,094 cm<sup>-1</sup> at 165 K. Finally, at 185 K, all CO has desorbed from the bare oxide surface<sup>25</sup>. Figure 1e repeats this procedure with 1% of a monolayer Pt coverage, at which Pt exists solely as single atoms. At 85 K, the oxide CO stretching bands are altered due to the presence of Pt, which is also seen in temperature-programmed desorption (TPD) experiments (Supplementary Fig. 2), leading to a more pronounced broad peak at 2,109 cm<sup>-1</sup>. As the surface is heated, desorption of CO from the oxide is complete and at 265 K the only signal remaining is at 2,028 cm<sup>-1</sup> due to CO on Pt single atoms. This CO desorbs by 325 K. The relative shifts in CO stretching frequencies are also captured very well by DFT, as shown by the listed values in Supplementary Table 1, which are also overlaid in the spectra in Supplementary Fig. 1.

**CO** oxidation activity of single Pt atoms and clusters. TPD was used to study the activity and mechanism of CO oxidation by Pt, as

shown in Fig. 2. Simultaneously acquired CO<sub>2</sub> and CO TPD traces at various Pt coverages are shown in Fig. 2a,b. All CO desorbs molecularly from the '29' oxide below 200 K under the experimental conditions<sup>25</sup>, such that in the absence of Pt (0%) no high-temperature CO or CO<sub>2</sub> desorption is detected. However, higher temperature desorption is seen when Pt is added to the surface. In the case of both CO<sub>2</sub> and CO desorption, as the Pt coverage is increased above 3% of a monolayer, the peak maximum shifts down in temperature, and a high-temperature shoulder forms that is consistent with Pt particle growth<sup>37-40</sup>. Low Pt coverages in the inset in Fig. 2a,b reveal that the CO and CO<sub>2</sub> desorption peaks are first-order in shape and do not shift with a change in Pt coverage, indicating that there are negligible lateral interactions due to high dispersion of single Pt atoms in this coverage regime, as was found by RAIRS. Figure 2a shows that single Pt atoms yield CO<sub>2</sub> with a peak maximum at 345 K and a CO desorption peak at 350 K. Importantly, CO is more weakly bound to single Pt atoms than to extended Pt surfaces and nanoparticles, which is a promising attribute in terms of resilience towards CO poisoning, which Pt clusters suffer from<sup>41</sup>. As such, CO oxidation occurs at temperatures that are well below the 425 K target required to meet future emission regulations<sup>42</sup>.

# Probing the CO oxidation mechanism with isotope labelling.

To probe the reaction mechanism, the '29' oxide support was labelled with 18O, as shown in Fig. 2d. Pt atoms at a concentration of 1% of a monolayer were deposited onto the support and the surface was then saturated with  $C^{16}O$ . The resulting desorption products were monitored and the CO<sub>2</sub> formed was exclusively m/z 46, which is direct evidence of a Mars-van Krevelen oxidation mechanism<sup>43</sup>, in which a single lattice oxygen from the Cu<sub>2</sub>18O-like support is extracted by C16O to form C16O18O. CO desorption and oxidation occur at similar temperatures with a  $33 \pm 2\%$  conversion to  $CO_2$ . A Redhead analysis of the CO desorption trace in Fig. 2d indicates that the barrier to CO desorption from Pt atoms is 1.1 eV, assuming a 10<sup>15</sup> s<sup>-1</sup> pre-exponential factor<sup>44</sup>. The oxidation of CO by single Pt atoms has an activation barrier of  $1.0 \pm 0.1$  eV, as found by complete analysis (Supplementary Fig. 3)45. After reaction, the surface is inactive toward CO oxidation, which cannot be attributed to sintering, as both TPD and RAIRS experiments show that no active surface NATURE CATALYSIS ARTICLES

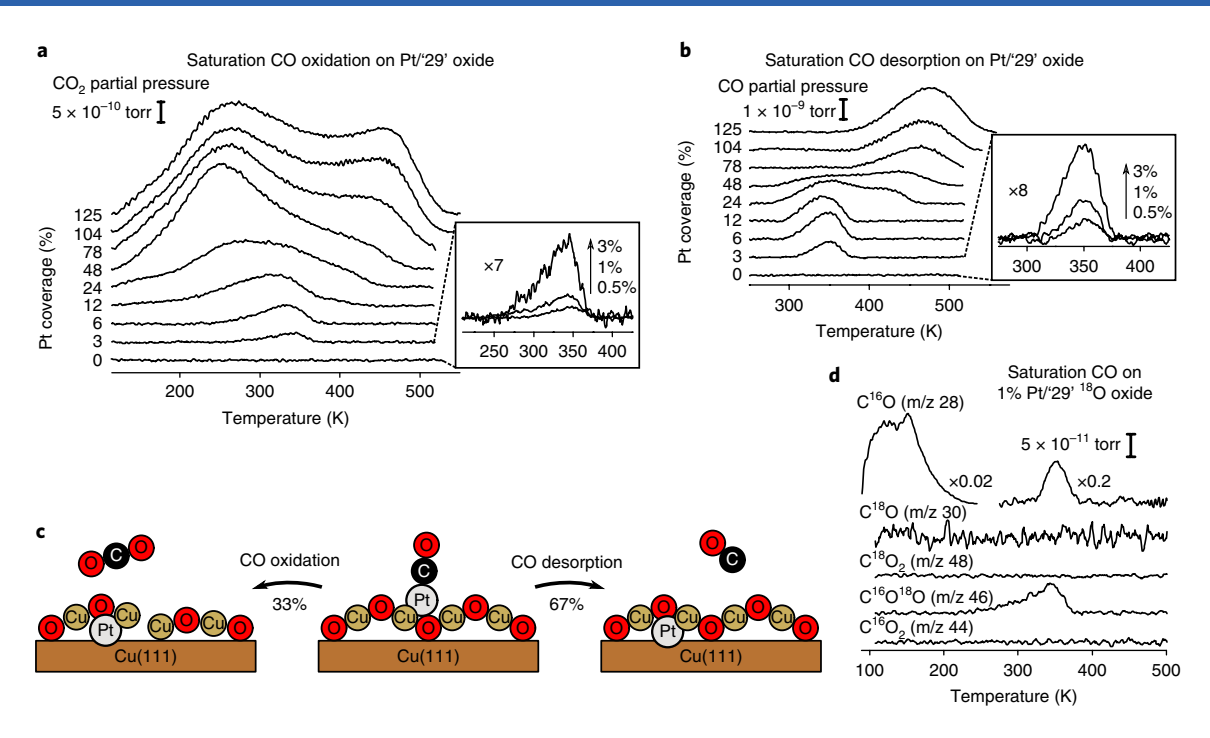


**Fig. 2 | TPD studies of CO oxidation by Pt supported on the '29' copper oxide. a**, A family of TPD curves of CO<sub>2</sub> (m/z 44) desorption from saturation CO coverages at different Pt coverages on the '29' oxide. **b**, A family of TPD curves of CO (m/z 28) desorption from the same experiments as in **a**. The insets highlight low Pt coverages at which Pt exists as isolated atoms. **c**, Schematic of the competing pathways for CO oxidation and CO desorption. **d**, TPD after saturation C¹6O exposure on a monolayer with 1% Pt coverage supported on an ¹8O-labelled '29' oxide.

Pt species remain after the reaction (Supplementary Fig. 2). A supported Pt atom has a high surface free energy relative to the '29' oxide; therefore, a thermodynamic driving force exists for the Pt to diffuse below the surface layer, where it cannot bind reactants, meaning that the active site is metastable. The diffusion of Pt below the surface occurs at high temperatures, and is separate from the oxidation reaction. After Pt deactivation, Pt is still atomically dispersed, but at sites that are not active—a result that would be very difficult to conclude using typical characterization techniques in a realistic catalytic system. Schematic representations of CO desorption and oxidation, both of which lead to Pt diffusion below the oxide surface, are shown in Fig. 2c.

## Atomic-scale imaging of active sites before and after reaction.

STM imaging allows for visualization of the atomic-scale structure of the surface around the Pt sites as the reaction progresses, as shown in Fig. 3. After the addition of 0.5% of a monolayer Pt coverage, the sample was saturated with CO and then annealed to 160 K to desorb CO from the oxide support<sup>25</sup>. As shown in Fig. 3a, the resulting surface is composed of single Pt atoms with CO adsorbed, in agreement with RAIRS data. It can also be seen that the Pt atoms are bound to different sites on the '29' oxide surface, probably giving rise to their variation in apparent height in the STM images. In Fig. 3b, the same surface was annealed to 250 K. STM shows that annealing has induced mobility of the CO-Pt units, as the majority  $(83 \pm 4\%)$  are now located at a single preferred binding site on the oxide. It has been previously shown that CO adsorption to single atoms can greatly enhance their lateral mobility on surfaces 20,21,32. At 250 K, CO<sub>2</sub> desorption begins to occur (Fig. 2d). The majority of Pt atoms retain their CO at this temperature, but some have reacted. In Fig. 3b, there are two Pt atoms at this preferred site and, importantly, new defects in the oxide adjacent to Pt atoms are seen that were not observed before annealing. This is highlighted by white arrows. As confirmed by the isotopic labelling TPD studies, these defects arise from lattice oxygen removal, and STM indicates that this occurs at sites that are adjacent to the active Pt. These Pt atoms also measure ~20 pm lower than the Pt atoms with CO adsorbed, indicating that these are post-reaction Pt sites. After the 250 K anneal,  $11 \pm 2\%$  of the Pt atoms have defects next to them where lattice oxygen has been removed. In Fig. 3c, a post-reaction image of the surface after a 350 K anneal is shown. On this surface, the area density of Pt is the same, indicating that the Pt is still dispersed; however, it no longer occupies the same preferred binding site seen in Fig. 3b. More Pt features are accompanied by defects in the '29' oxide after annealing to 350 K due to the formation of more CO<sub>2</sub> at this higher temperature. However, not all Pt atoms are adjacent to defects, which is consistent with the TPD results and indicates competition between CO desorption and oxidation, as observed for Pt supported on CuO/Cu(110), where Pt single atoms are not active for low-temperature CO oxidation<sup>22</sup>. STM analysis indicates that  $42 \pm 12\%$  of Pt atoms are adjacent to a defect, in agreement with the  $33 \pm 2\%$  CO<sub>2</sub> yield found by TPD.

STM and DFT were used to identify the preferred binding site for the active CO-Pt unit after a 250 K anneal (Fig. 3d,f,g). Due to the large size of the '29' oxide unit cell<sup>24,25</sup>, there are many possible binding sites for Pt on the surface. By benchmarking each possible Pt site against the experimental findings, we were able to reduce the number of Pt active site candidates from 24 to a single site that matched the experimental criteria (see Supplementary Information). In Fig. 3f, the CO-Pt binding site is highlighted by the blue circle (see also Fig. 3d). This area was mapped onto the previously proposed atomic structure of the support<sup>24,25</sup>. In Fig. 3f, the unit cell is also marked with numeric labels for the possible Pt binding sites on the '29' oxide. The structure shown in Fig. 3g is the CO-Pt unit at site 18, which our analysis determined to be the best candidate for the active Pt site. At this site the CO molecule is leaning down and to the right, putting its highest topographical point very close to the centre of the blue circle, making it an excellent match with the experimental data. In the DFT model, the binding strength of CO is consistent with the TPD experiments (Supplementary Fig. 4). At

ARTICLES NATURE CATALYSIS

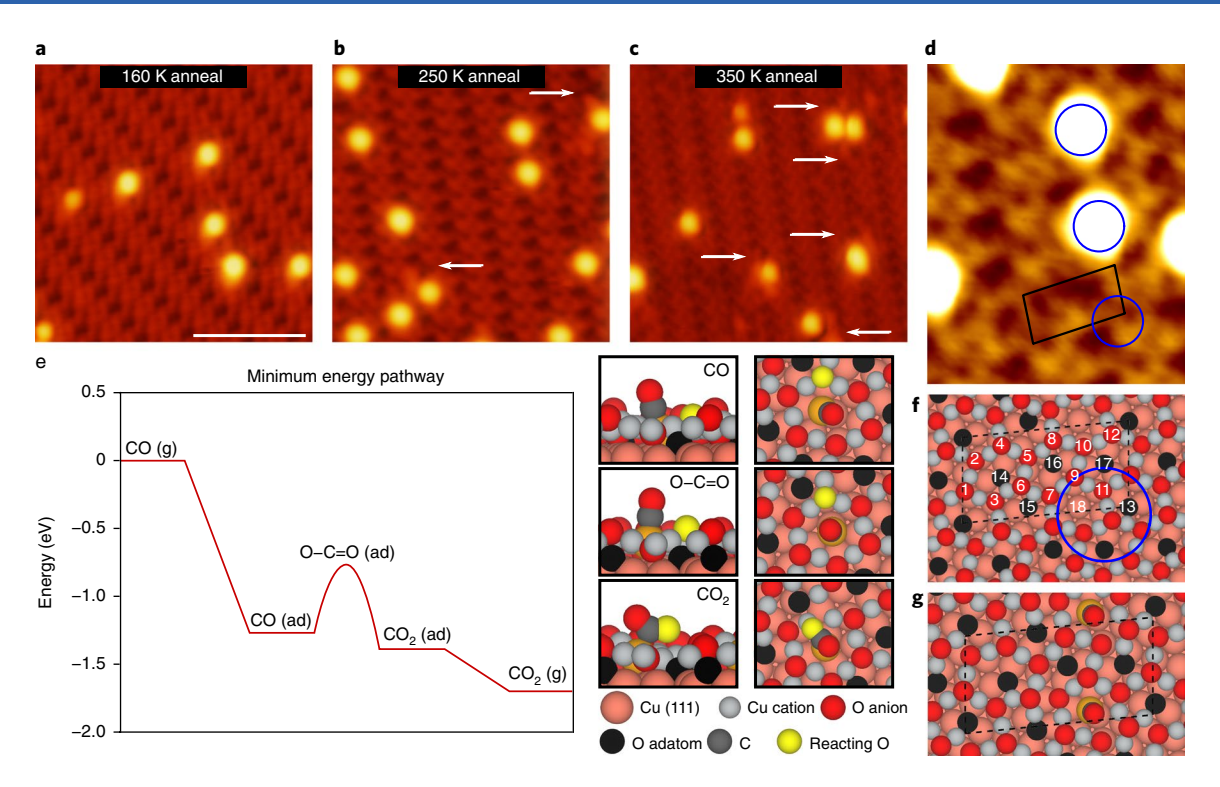


**Fig. 3 | Visualization of the CO oxidation mechanism by STM and rationalization by DFT. a-c**, 5 K high-resolution STM image of CO-exposed Pt atoms supported on the '29' oxide after annealing at 160 K (**a**; scale bar: 5 nm), 250 K (**b**) and 350 K (**c**). White arrows highlight defects arising from the removal of lattice oxygen in the reaction. **d**, High-resolution STM image of CO-Pt annealed at 250 K. The blue circle highlights the preferred CO-Pt site. The black outline shows the unit cell of the support. **e**, DFT-calculated MEP for the oxidation of CO on the model Pt single-atom active site supported on the '29' oxide surface, where '(g)' indicates that the molecule is in the gas phase and '(ad)' indicates that it is adsorbed. **f**, Atomic model of the '29' oxide support with the blue circle from **d** overlaid. All possible adsorption sites for a single Pt atom on the '29' oxide model surface are labelled numerically. **g**, DFT-calculated lowest-energy structure for a CO-Pt unit in the blue circle indicated in **f**.

this site, the adsorbed CO could be oxidized by any of six lattice oxygen atoms in the surrounding Cu<sub>2</sub>O ring (Supplementary Fig. 5). The reactions of adsorbed CO with each lattice oxygen to form gas-phase CO<sub>2</sub> had reaction energies ranging from 0.36 to -0.44 eV (Supplementary Fig. 5). Activation energies were calculated to determine whether CO oxidation is likely to occur on the supported Pt single atoms. The minimum energy pathway (MEP) for adsorbed CO on the Pt single atom reacting with the most favourable lattice oxygen was calculated and is shown in Fig. 3e. The MEP has a moderate barrier for the oxidation of adsorbed CO to CO<sub>2</sub>. The bond breaking of Cu-O<sub>lattice</sub> is part of the transition state that involves O<sub>lattice</sub> and the adsorbed CO. The rate-limiting nature of the firstorder elementary step of breaking the Cu-O<sub>lattice</sub> bond explains the experimental CO<sub>2</sub> desorption trace (Fig. 2a) exhibiting the characteristic shape of first-order desorption. Furthermore, desorption of CO<sub>2</sub> from the Pt single atom is calculated to be both barrierless and exothermic. DFT calculations of the complete CO oxidation reaction cycle (Supplementary Fig. 5) also indicate that CO<sub>2</sub> formation has the largest reaction barrier. Overall, the DFT-calculated MEP for CO oxidation via a Mars-van Krevelen mechanism is consistent with the experimental TPD, and further shows that atomically dispersed Pt atoms on the '29' oxide are active and the lattice oxygen in close vicinity to the Pt atom is removed in the reaction.

Charge state of single Pt atom active sites. X-ray photoelectron spectroscopy (XPS) experiments were carried out to investigate the charge state of single Pt atoms at a coverage of 2% of a monolayer during the CO oxidation reaction (Fig. 4a). Pt grown on metallic Cu(111) was used as a reference for the Pt  $4d_{5/2}$  peak. In the case of as-prepared Pt on the '29' oxide support at 150 K (green), the peak is notably very broad, consistent with an averaging of Pt species at dif-

ferent binding sites on the surface. XPS identifies Pt as charge neutral, with the peak centred near the same binding energy as found for Pt(0). The surface was then annealed at 250 K (magenta), for which the XPS peak remains at the same binding energy. Next, the impact of CO exposure was studied (red). Pt and CO were deposited and annealed at 250 K, and a narrowing of the peak was found, consistent with diffusion of CO–Pt complexes to one of the preferred binding sites. Finally, the sample was annealed at 350 K (blue), for which the Pt  $4d_{5/2}$  XPS peak remains mostly unchanged. The neutral charge of Pt is also consistent with the lower CO stretch frequency found by RAIRS, and agrees with the DFT model (Supplementary Fig. 6).

It is surprising to find that single Pt atoms in a neutral charge state can oxidize CO, as most supported single-atom catalyst studies report the catalytic atom to be charged1-4. To further investigate the chemical nature of Pt single atoms bound to CO, highly accurate partial density of states (PDOS) were generated from our DFT model system and were compared with the normalized conductance of the active CO-Pt surface sites measured experimentally by STM (Supplementary Fig. 7 and Fig. 4b)46,47. The agreement between the two curves indicates that the electronic states calculated by DFT are present in the active Pt atoms studied experimentally. The atomic orbital contributions to the PDOS are shown in Fig. 4c, in which DFT shows that the state centred around  $-1.5 \,\mathrm{V}$  is a Pt d state. Integration of the DFT-based 6s and 5d states of the Pt atom to the Fermi level yielded 1.0 and 8.9 electrons in these orbitals, respectively, which agrees with the XPS results indicating that the Pt atoms are neutral, and is in accordance with previous results on thin oxide films<sup>14,48</sup>. It has been proposed that neutral Pt is more active than cationic Pt9,49, but generally, neutral Pt exists in nanoparticles while cationic Pt exists as single atoms, making it impossible to assign reactivity to the charge state alone. While neutral single atoms have been identified

NATURE CATALYSIS ARTICLES

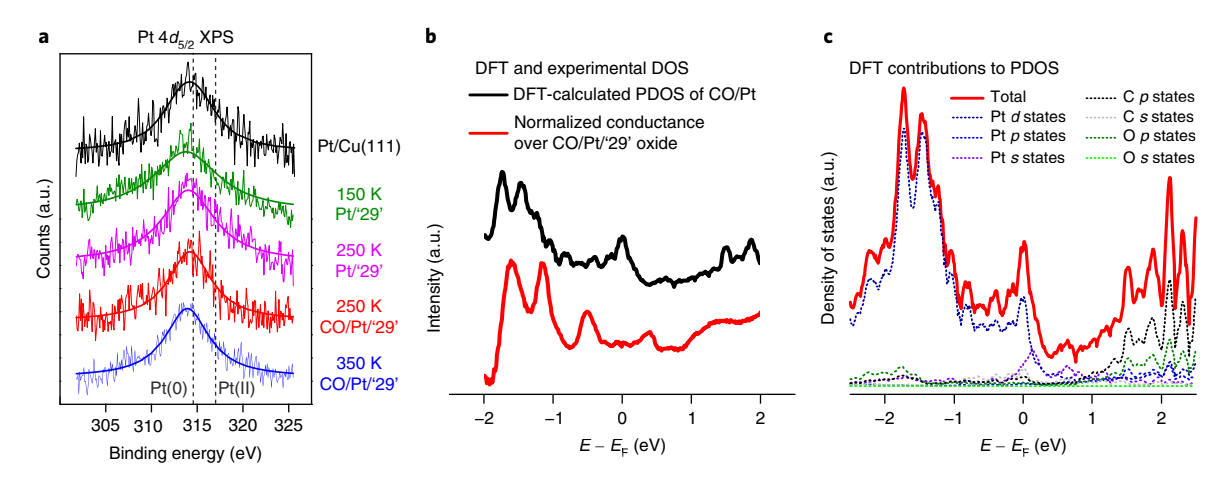


**Fig. 4 | Electronic structure characterization of oxide-supported Pt atoms. a**, XPS data showing the Pt  $4d_{5/2}$  peak for a set of surfaces with 2% of a monolayer Pt coverage, with literature values for Pt(O) and Pt(II) displayed for reference. **b**, Comparison of calculated PDOS and experimental normalized conductance over the CO/Pt site. **c**, Breakdown of contributions from different states of Pt, C and O to the CO-Pt total PDOS. *E* is energy and  $E_F$  is the Fermi level.

before<sup>31,50</sup>, it is not well understood how the charge state of an isolated atom impacts its catalytic activity and stability. In the present system the effect of Pt nanoparticles can be conclusively ruled out, and neutral single Pt atoms are shown to indeed be active for CO oxidation.

### **Conclusions**

In conclusion, we have used a well-defined model system with mono-disperse Pt atoms in which the atomic-scale geometry and electronic structure of the active sites can be directly probed and correlated to CO oxidation activity. Active Pt single atoms exist in highly uniform sites on the '29' copper oxide support. The reaction proceeds via a Mars-van Krevelen mechanism on the reducible oxide surface, in which lattice oxygen in close vicinity to the Pt sites is involved in the oxidation process, as confirmed by STM, TPD, and theory. Complementary RAIRS measurements allow the unambiguous assignment of CO stretching frequencies at single Pt atoms. This work serves as a benchmark for the characterization of single Pt atom catalysts by infrared spectroscopy. It also provides new insight into the deactivation mechanism of Pt atoms, which was not caused by sintering, but rather by the embedding of the individual Pt atoms into the support. While STM imaging reveals that the atoms are still highly dispersed in this deactivated state, they cannot access reactants, which is an important consideration in the study of real catalysts. This is in contrast with the more typical deactivation mechanism caused by sintering. Taken together, these results indicate that single supported Pt atoms are capable of performing catalytically relevant reaction steps, but the nature of the active site (that is, clusters or single atoms) will depend on the oxide support under consideration. Furthermore, our investigation shows that Pt single atoms exist in a neutral charge state not previously considered to be present or active at the single atom limit on a surface oxide support.

### Methods

TPD. TPD experiments were carried out in an ultra-high vacuum (UHV) chamber with a base pressure of  $<1\times10^{-10}\,\rm mbar$ . The chamber was equipped with a quadrupole mass spectrometer (Hiden) and the Cu(111) crystal was able to be cooled to 85 K with liquid nitrogen and resistively heated to 750 K. The Cu(111) crystal was cleaned by Ar^+ sputtering and annealing to 750 K. The '29' oxide film was formed by exposure to O<sub>2</sub> gas (USP Grade; Airgas) or  $^{18}\text{O}_2$  (97%; Aldrich) at a pressure of  $5\times10^{-6}\,\rm mbar$  for 3 min at a sample temperature of  $650\pm20\,\rm K$ . The formation of the '29' oxide was verified by low-energy electron diffraction (OCI Vacuum Microengineering). Pt depositions were performed on a cooled '29' oxide sample held at 85 K, using a Focus GmbH EFM3 electron beam evaporator. One monolayer is defined as the packing density of Cu(111),  $1.77\times10^{15}\,\rm atoms\,cm^{-2}$ . High precision leak valves allowed for accurate exposure of CO (99.99%; Airgas). TPD experiments were performed with a linear heating ramp of 1 K s^{-1}. Quantitative analysis of TPD

peak area included factors for the ionization cross section of desorbing species, their fragmentation pattern and the quadrupole mass spectrometer sensitivity.

STM. For the STM experiments the sample was prepared in a preparation chamber (pressure,  $P = 2 \times 10^{-10}$  mbar) following the same protocol as in the TPD experiments. The sample was then transferred in a UHV to the STM chamber  $(P=1\times10^{-11} \text{ mbar})$  and into the pre-cooled 5 K STM stage. CO was deposited onto the 5K surface using line-of-sight molecular dosers installed on the STM chamber. The sample was then annealed to various temperatures and cooled back to 5 K before imaging was conducted using a low-temperature Omicron NanoTechnology STM. The defect density of the as-prepared '29' oxide is very low, with a surface coverage of  $\sim 0.02\%$  of a monolayer with respect to Cu(111)<sup>24</sup>. Images were acquired using an etched W tip. Imaging conditions in the presented data are -0.5 V, with respect to the sample, and 0.5 nA. For scanning tunnelling spectroscopy (STS) experiments, all normalized conductance spectra were generated from dI/dV measurements using a lock-in amplifier set with a sinusoidal modulation frequency of 6.75 kHz and 4 mV amplitude added to the sample bias. The dI/dV spectra were recorded with the feedback loop open and blanked at 2 V and 10 nA. The voltage was swept from +2 to −2 V over 300 points with a T-raster of 30 ms, and the I/V spectra were recorded simultaneously. The presented spectrum is the normalized conductance  $\left(\frac{V}{I}\frac{dI}{dV}\right)$  (refs <sup>46,47</sup>) averaged over 22 background spectra on the oxide and 43 CO-Pt spectra all recorded in alternating succession with the same STM tip.

**XPS.** XPS experiments were performed in a UHV using a cryogenically cooled manipulator. The sample preparation followed the same previously described protocol. The XPS (PSP Vacuum Technology) was operated using an Al K $\alpha$  photon source (1,486.6 eV) and hemispherical electron analyser set to a constant pass energy of 50 eV. Spectra were shifted to align the Cu  $2p_{3/2}$  peak to a binding energy of 933 eV. The presented XPS data have a step size of 0.1 eV and Shirley background subtractions have been applied. XPS peaks were analysed by fits with Voigt-type line shapes.

RAIRS. RAIRS experiments were performed with an out-of-vacuum Bruker Fourier transform infrared source and liquid-nitrogen-cooled mercury cadmium telluride detector, with a reflection angle of 5° to the sample. The sample was in a UHV chamber, and infrared light travelled in and out of UHV through sapphire windows. All sample preparation followed the same procedures as above. The bare '29' oxide surface at room temperature was used as the background spectra. All spectra are presented as raw data without any smoothing, aside from the 1% of a monolayer of Pt spectrum in which a Savitzky–Golay smoothing filter, fitting a second-order polynomial to 8 cm<sup>-1</sup> windows, was applied to reduce the noise. Spectra were taken at a resolution of 2 cm<sup>-1</sup> averaged over 32 scans with a scanner velocity of 3.75 KHz. The Blackman–Harris 3-Term apodization function was applied using a zero-filling factor of 2.

**DFT.** The DFT calculations performed here utilized the Vienna ab initio simulation package code<sup>81,52</sup> where the core electrons were treated with the projector augmented wave method<sup>83,54</sup>. The valence electrons for all systems were described using the generalized gradient approximation with the Perdew—Burke—Ernzerhof functional<sup>55</sup>. The energy cutoff for the plane-wave basis set was set to 500 eV, and the electron smearing was described by the Gaussian smearing method with a width of 0.2 eV. All surface calculations were performed using a

ARTICLES NATURE CATALYSIS

 $1 \times 2 \times 1$  Monkhorst–Pack k-points mesh<sup>56</sup>. The details of the construction and verification of the surface model of '29' oxide support have been thoroughly investigated elsewhere<sup>24,25</sup>, and the resulting '29' oxide support model is used here. The adsorption energy of CO on the Pt single atoms was calculated according to:

$$E_{\text{ads}} = \frac{E_{\text{nCO/S}} - E_{\text{S}} - nE_{\text{CO}}}{n} \tag{1}$$

where  $E_{n CO(S)}$   $E_{s}$  and  $E_{CO}$  are the total energies of the CO-adsorbed supported Pt single-atom surface, clean supported Pt single-atom surface and gas-phase CO, while n is the number of CO molecules adsorbed on the surface. The high-accuracy PDOS calculated for this system was generated using the method of refs  $^{57,58}$ , which fits an atom centred basis set of Slater-type orbitals to the total wave function generated by the Vienna ab initio simulation package. For the PDOS presented here, the states below the Fermi level were captured with an error in the resulting total wave function of less than 2%.

Each ground-state optimization calculation was considered converged when the total energy changed by less than 10<sup>-6</sup> eV, and the forces between atoms were smaller than 0.02 eV/Å. The transition states were investigated using the nudged elastic band method<sup>59</sup> to pre-converge the MEP to a total energy accuracy of 10-4 eV and interatomic forces of less than 0.1 eV/Å. This MEP was then converged using the climbing image nudged elastic band method60 to a total energy accuracy of  $10^{-6}\,\text{eV}$  and interatomic forces of less than  $0.05\,\text{eV/Å}$ . The presence of a transition state was verified by calculating the vibrational modes for the highest energy structure in the climbing image nudged elastic band optimized MEP and ensuring that there was a single imaginary mode<sup>61</sup>. Additionally, the DFT-based STM image was generated using the method discussed in our previous work  $^{24,25}$ . Tests of the functional effect on the DFT-calculated activation and reaction engeries were performed using the RPBE62 and vdW-DF63 functionals, as well as the DFT+U method  $^{64}$  with U values ranging from 0 to 5 eV applied to the d states of the Cu oxide species (see Supplementary Information). For the tests using the RPBE and vdW-DF functionals, the Cu lattice constant was optimized and found to be 3.680 and 3.705 Å, respectively. For the DFT+U scan, the Cu lattice constant was kept at the value optimized with the Perdew-Burke-Ernzerhof functional, which is 3.635 Å.

Pt slab models were used here in addition to the '29' oxide support to provide benchmarks for the CO adsorption energy, Pt 4d XPS and CO vibrational analyses. A p(4×4) Pt(111) surface was used for the CO adsorption energy and Pt 4d XPS analyses to simulate the low coverage limit for both CO and a single, excited Pt surface atom. The CO vibrational modes were benchmarked against those calculated for the  $c(4\times2)$  CO overlayer structure on Pt(111). In both Pt(111) models, the surfaces were modelled with 5 atomic layers, with only the top two allowed to relax during optimization, and the vacuum spacing was at least  $14\,\text{Å}$ . The bulk Pt lattice constant was calculated to be  $3.980\,\text{Å}$ .

**Data availability.** The data that support the plots within this paper and other findings of this study are available from the authors upon reasonable request.

Received: 16 May 2017; Accepted: 24 January 2018; Published online: 05 March 2018

### References

- Thomas, J. M. The concept, reality and utility of single-site heterogeneous catalysts (SSHCs). Phys. Chem. Chem. Phys. 16, 7647–7661 (2014).
- Liu, J. Catalysis by supported metal single atoms. ACS Catal. 7, 34–59 (2017).
- Flytzani-Stephanopoulos, M. & Gates, B. C. Atomically dispersed supported metal catalysts. Annu. Rev. Chem. Biomol. Eng. 3, 545–574 (2012).
- Nie, L. et al. Activation of surface lattice oxygen in single-atom Pt/CeO<sub>2</sub> for low-temperature CO oxidation. Science 358, 1419–1423 (2017).
- Yang, M. et al. Catalytically active Au–O(OH)<sub>x</sub>-species stabilized by alkali ions on zeolites and mesoporous oxides. Science 346, 1498–1501 (2014).
- Yang, M. et al A common single-site Pt(II)-O(OH)x—species stabilized by sodium on 'active' and 'inert' supports catalyzes the water-gas shift reaction. J. Am. Chem. Soc. 137, 3470–3473 (2015).
- Zhai, Y. et al. Alkali-stabilized Pt-OH<sub>x</sub> species catalyze low-temperature water-gas shift reactions. Science 329, 1633–1636 (2010).
- Hutchings, G. J. et al. Role of gold cations in the oxidation of carbon monoxide catalyzed by iron oxide-supported gold. J. Catal. 242, 71–81 (2006)
- Liu, S. et al. Stabilizing single-atom and small-domain platinum via combining organometallic chemisorption and atomic layer deposition. Organometallics 36, 818–828 (2017).
- Ding, K. et al. Identification of active sites in CO oxidation and water-gas shift over supported Pt catalysts. Science 350, 189–192 (2015).
- Herzing, A. A., Kiely, C. J., Carley, A. F., Landon, P. & Hutchings, G. J. Identification of active gold nanoclusters on iron oxide supports for CO oxidation. Science 321, 1331–1335 (2008).

- Ulrich, S. et al. Evidence for a size-selective adsorption mechanism on oxide surfaces: Pd and Au atoms on SiO<sub>2</sub>/Mo(112). ChemPhysChem 9, 1367–1370 (2008).
- 13. Bliem, R. et al. Cluster nucleation and growth from a highly supersaturated adatom phase: silver on magnetite. ACS Nano 8, 7531–7537 (2014).
- Giordano, L. et al. Charging of metal adatoms on ultrathin oxide films: Au and Pd on FeO/Pt(111). Phys. Rev. Lett. 101, 26102 (2008).
- Novotný, Z. et al. Ordered array of single adatoms with remarkable thermal stability: Au/Fe<sub>3</sub>O<sub>4</sub>(001). Phys. Rev. Lett. 108, 216103 (2012).
- Skomski, D., Tempas, C. D., Smith, K. A. & Tait, S. L. Redox-active on-surface assembly of metal—organic chains with single-site Pt(II). *J. Am. Chem. Soc.* 136, 9862–9865 (2014).
- Skomski, D. et al. Two- and three-electron oxidation of single-site vanadium centers at surfaces by ligand design. *J. Am. Chem. Soc.* 137, 7898–7902 (2015).
- Rim, K. T. et al. Charging and chemical reactivity of gold nanoparticles and adatoms on the (111) surface of single-crystal magnetite: a scanning tunneling microscopy/spectroscopy study. J. Phys. Chem. C 113, 10198–10205 (2009).
- Yang, B., Lin, X., Gao, H.-J., Nilius, N. & Freund, H.-J. CO adsorption on thin MgO films and single Au adatoms: a scanning tunneling microscopy study. J. Phys. Chem. C 114, 8997–9001 (2010).
- 20. Parkinson, G. S. et al. Carbon monoxide-induced adatom sintering in a Pd-Fe<sub>3</sub>O<sub>4</sub> model catalyst. *Nat. Mater.* **12**, 724–728 (2013).
- Bliem, R. et al. Dual role of CO in the stability of subnano Pt clusters at the Fe<sub>3</sub>O<sub>4</sub>(001) surface. Proc. Natl Acad. Sci. USA 113, 8921–8926 (2016).
- Zhou, X. et al. Stable Pt single atoms and nanoclusters on ultrathin CuO film and their performances in CO oxidation. J. Phys. Chem. C 120, 1709–1715 (2016).
- Bliem, R. et al. An atomic-scale view of CO and H<sub>2</sub> oxidation on a Pt/Fe<sub>3</sub>O<sub>4</sub> model catalyst. Angew. Chem. Int. Ed. Engl. 54, 13999–14002 (2015).
- Therrien, A. J. et al. Structurally accurate model for the '29'-structure of Cu<sub>x</sub>O/Cu(111): a DFT and STM study. J. Phys. Chem. C 120, 10879–10886 (2016)
- Hensley, A. J. R. et al. CO adsorption on the '29' Cu<sub>x</sub>O/Cu(111) surface: an integrated DFT, STM and TPD study. J. Phys. Chem. C 120, 25387–25394 (2016).
- Mukerji, R. J., Bolina, A. S. & Brown, W. A. A RAIRS and TPD investigation of the adsorption of CO on Pt{211}. Surf. Sci. 527, 198–208 (2003).
- Hayden, B. E. & Bradshaw, A. M. The adsorption of CO on Pt(111) studied by infrared-reflection-adsorption spectroscopy. Surf. Sci. 125, 787–802 (1983).
- 28. Orita, H. & Inada, Y. DFT investigation of CO adsorption on Pt(211) and Pt (311) surfaces from low to high coverage. *J. Phys. Chem. B* **109**, 22469–22475 (2005).
- Lundwall, M. J., Mcclure, S. M. & Goodman, D. W. Probing terrace and step sites on Pt nanoparticles using CO and ethylene. *J. Phys. Chem. C* 114, 7904–7912 (2010)
- Hoffman, A. S., Fang, C.-Y. & Gates, B. C. Homogeneity of surface sites in supported single-site metal catalysts: assessment with band widths of metal carbonyl infrared spectra. J. Phys. Chem. Lett. 7, 3854–3860 (2016).
- Liu, L. et al. Generation of subnanometric platinum with high stability during transformation of a 2D zeolite into 3D. Nat. Mater. 16, 132–138 (2017).
- Matsubu, J. C., Yang, V. N. & Christopher, P. Isolated metal active site concentration and stability control catalytic CO<sub>2</sub> reduction selectivity. *J. Am. Chem. Soc.* 137, 3076–3084 (2015).
- Lee, H. & Ho, W. Structural determination by single-molecule vibrational spectroscopy and microscopy: contrast between copper and iron carbonyls. *Phys. Rev. B* 61, R16347–R16350 (2000).
- Chen, S. et al. Probing surface structures of CeO<sub>2</sub>, TiO<sub>2</sub>, and Cu<sub>2</sub>O nanocrystals with CO and CO<sub>2</sub> chemisorption. J. Phys. Chem. C 120, 21472–21485 (2016).
- Baber, A. E. et al. Stabilization of catalytically active Cu<sup>+</sup> surface sites on titanium-copper mixed-oxide films. *Angew. Chem. Int. Ed. Engl.* 126, 5440–5444 (2014).
- Baber, A. E. et al. In situ imaging of Cu<sub>2</sub>O under reducing conditions: formation of metallic fronts by mass transfer. J. Am. Chem. Soc. 135, 16781–16784 (2013).
- Gerrard, A. L. & Weaver, J. F. Kinetics of CO oxidation on high-concentration phases of atomic oxygen on Pt(111). J. Chem. Phys. 123, 224703 (2005).
- Heiz, U., Sanchez, A., Abbet, S. & Schneider, W.-D. Catalytic oxidation of carbon monoxide on monodispersed platinum clusters: each atom counts. J. Am. Chem. Soc. 121, 3214–3217 (1999).
- Xu, J. & Yates, J. T. Catalytic oxidation of CO on Pt(335): a study of the active site. J. Chem. Phys. 99, 725–732 (1993).
- Campbell, C. T., Ertl, G., Kuipers, H. & Segner, J. A molecular beam investigation of the interactions of CO with a Pt(111) surface. Surf. Sci. 107, 207–219 (1981).
- Liu, J. et al. Tackling CO poisoning with single-atom alloy catalysts. J. Am. Chem. Soc. 138, 6396–6399 (2016).

NATURE CATALYSIS ARTICLES

- 42. National Archives and Records Administration Greenhouse gas emissions and fuel efficiency standards for medium- and heavy-duty engines and vehicles—phase 2. Fed. Regist. 81, 73478–74274 (2016)..
- 43. Doornkamp, C. & Ponec, V. The universal character of the Mars and Van Krevelen mechanism. *J. Mol. Catal. A Chem.* **162**, 19–32 (2000).
- 44. Redhead, P. A. Thermal desorption of gases. Vacuum 12, 203-211 (1962).
- King, D. A. Thermal desorption from metal surfaces: a review. Surf. Sci. 47, 384–402 (1975).
- Koslowski, B., Dietrich, C., Tschetschetkin, A. & Ziemann, P. Evaluation of scanning tunneling spectroscopy data: approaching a quantitative determination of the electronic density of states. *Phys. Rev. B* 75, 35421 (2007).
- Lang, N. D. Spectroscopy of single atoms in the scanning tunneling microscope. *Phys. Rev. B* 34, 5947–5950 (1986).
- Giordano, L. & Pacchioni, G. Oxide film at the nanoscale: new structures, new functions, and new materials. Acc. Chem. Res. 44, 1244–1252 (2011).
- Jones, J. et al. Thermally stable single-atom platinum-on-ceria catalysts via atom trapping. Science 353, 150–154 (2016).
- Lang, R. et al. Hydroformylation of olefins by a rhodium single-atom catalyst with activity comparable to RhCl(PPh<sub>3</sub>)<sub>3</sub>. Angew. Chem. Int. Ed. Engl. 55, 16054–16058 (2016).
- Kresse, G. & Hafner, J. Ab initio molecular dynamics for liquid metals. *Phys. Rev. B* 47, 558–561 (1993).
- Kresse, G. & Furthmüller, J. Efficient iterative schemes for ab initio total-energy calculations using a plane-wave basis set. *Phys. Rev. B* 54, 11169–11186 (1996).
- Blochl, P. E. Projector augmented-wave method. *Phys. Rev. B* 50, 17953–17979 (1994).
- Kresse, G. & Joubert, D. From ultrasoft pseudopotentials to the projector augmented-wave method. *Phys. Rev. B* 59, 1758–1775 (1999).
- Perdew, J. P., Burke, K. & Ernzerhof, M. Generalized gradient approximation made simple. *Phys. Rev. Lett.* 77, 3865–3868 (1996).
- Pack, J. D. & Monkhorst, H. J. Special points for Brillouin-zone integrations. Phys. Rev. B 13, 5188–5192 (1976).
- Deringer, V. L., Tchougréeff, A. L. & Dronskowski, R. Crystal orbital Hamilton population (COHP) analysis as projected from plane-wave basis sets. J. Phys. Chem. A 115, 5461–5466 (2011).
- Maintz, S., Deringer, V. L., Tchougréeff, A. L. & Dronskowski, R. Analytic projection from plane-wave and PAW wavefunctions and application to chemical-bonding analysis in solids. J. Comput. Chem. 34, 2557–2567 (2013).
- Henkelman, G. & Jónsson, H. A dimer method for finding saddle points on high dimensional potential surfaces using only first derivatives. *J. Chem. Phys.* 111, 7010–7022 (1999).
- Henkelman, G., Überuaga, B. P. & Jónsson, H. Climbing image nudged elastic band method for finding saddle points and minimum energy paths. *J. Chem. Phys.* 113, 9901–9904 (2000).
- Trygubenko, S. A. & Wales, D. J. A doubly nudged elastic band method for finding transition states. J. Chem. Phys. 120, 2082–2094 (2004).

- Hammer, B., Hansen, L. B. & Nørskov, J. K. Improved adsorption energetics within density-functional theory using revised Perdew–Burke–Ernzerhof functionals. *Phys. Rev. B* 59, 7413–7421 (1999).
- Dion, M., Rydberg, H., Schröder, E., Langreth, D. C. & Lundqvist, B. I. Van der Waals density functional for general geometries. *Phys. Rev. Lett.* 92, 246401 (2004).
- 64. Dudarev, S. L., Savrasov, S. Y., Humphreys, C. J. & Sutton, A. P. Electron-energy-loss spectra and the structural stability of nickel oxide: an LSDA+U study. *Phys. Rev. B* 57, 1505–1509 (1998).

# Acknowledgements

The surface science work at Tufts was supported by the Department of Energy Basic Energy Sciences programme under grant number DE-FG02-05ER15730. M.D.M. thanks Tufts Chemistry for an Illumina Fellowship. Financial support at Washington State University was provided by the National Science Foundation Early-concept Grants for Exploratory Research programme under contract number CBET-1552320 and the CAREER programme under contract number CBET-1653561. Our thanks also go to the donors of the American Chemical Society Petroleum Research Fund. A portion of the computer time for the computational work was performed at the Environmental Molecular Sciences Laboratory—a national scientific user facility sponsored by the Department of Energy's Office of Biological and Environmental Research and located at the Pacific Northwest National Laboratory. The Pacific Northwest National Laboratory operated for the US Department of Energy by Battelle.

### **Author contributions**

A.J.T. carried out the sample preparation as well as the STM, STS, TPD, XPS and RAIRS experiments, and assisted with writing the manuscript. A.J.R.H. carried out the DFT calculations and assisted with writing the manuscript. M.D.M. assisted with the TPD and STM experiments. R.Z. assisted with the DFT calculations. F.R.L. assisted with the STM imaging and STS experiments. B.C. and A.C.S. assisted with the STM imaging and XPS experiments. J.-S.M. oversaw and guided the DFT calculations and assisted with writing the manuscript. E.C.H.S. conceived the project, directed the study and assisted with writing the manuscript.

### Competing interests

The authors declare no competing interests.

### Additional information

**Supplementary information** is available for this paper at https://doi.org/10.1038/s41929-018-0028-2.

Reprints and permissions information is available at www.nature.com/reprints.

Correspondence and requests for materials should be addressed to J.-S.M. or E.C.H.S.

**Publisher's note:** Springer Nature remains neutral with regard to jurisdictional claims in published maps and institutional affiliations.